Nonlinear Dyn
https://doi.org/10.1007/s11071-024-09936-7

ORIGINAL PAPER

Neural modeling of power nonlinear inductors by the E-αNet network

Giovanni Pilato · Gianpaolo Vitale · Giorgio Vassallo · Daniele Scirè

Received: 12 June 2023 / Accepted: 24 June 2024

Abstract In this paper, a model for nonlinear ferrite power inductors based on the αNet neural network is proposed. The model is able to reproduce the ferrite power inductors inductor behavior up to saturation, considering the core temperature. The αNet neural network was used for its generalization capability considering a hybrid approach encompassing a classical weighted interpolation. The model's effectiveness was experimentally verified by calculating the current flowing through two inductors in an electric circuit in different operating conditions, and has been compared with the two main models found in literature to show the improvement both in terms of the maximum value of the estimated current and the root mean square error. The modeling procedure can be easily extended to inductors with different sizes and core materials due to the features of the αNet network and the hybrid approach to retrieve data.

G. Pilato · G. Vitale (✉)
ICAR-CNR, Via Ugo la Malfa 153, Palermo, Italy
e-mail: gianpaolo.vitale@icar.cnr.it

G. Pilato
e-mail: giovanni.pilato@icar.cnr.it

G. Vassallo · D. Scirè
Department of Engineering, University of Palermo, 90128 Palermo, Italy
e-mail: giorgio.vassallo@unipa.it

D. Scirè
e-mail: daniele.scire@unipa.it

Published online: 15 July 2024

Keywords Neural model · Nonlinear inductor · Switched mode power supply · Saturable core

1 Introduction

The dynamics of power converters are of deep interest for scientists dealing with power electronics since they show many aspects related to nonlinear behavior; among these aspects are bifurcation [1] and chaos [2], while others affect control systems [3,4]. Finally, issues are related to circuit models [5,6]. It is noteworthy that most of the published papers dealing with power converters are based on traditional inductors, i.e., they consider its inductance as a constant value. Recently, nonlinear power inductors have been used in electronics applications [7] dealing with electrical vehicles [8] or in switched mode power supplies (SMPSs) [9]. Recent reports have shown that the operating range of a power inductor can be extended up to the saturation value, indicating that the operating current can be raised up to the value at which the inductance is halved; this allows saving cost and weight of the inductor [8]. This operating mode improves the power density; hence, it is of great interest in practical applications, particularly concerning SMPSs either for grid-connected applications [10], or for DC/DC conversion [11,12]. On the other hand, the theoretical analysis is more complicated since, by increasing the current, the inductor exhibits a nonlinearity that depends on the core magnetic material [13]; consequently, the inductance is not constant, it

shows an abrupt fall and tends to an asymptotic behavior up to the deep saturation value. Simulation analysis of the current through the inductor is essential because this current also affects other devices connected with the inductor (power switch and diode) [14]; toward this end, a reliable model for calculating the inductor current for any given applied voltage up to saturation and considering the core temperature is needed. In addition, during the design phase, it is necessary to use such a model to predict the electromagnetic interference (EMI) generated by the circuit system and minimize it by suitable filters facing issues related to components search [15], traditional design [16] and optimized techniques [17]. Finally, a proper inductor model must show good performance in terms of accuracy and a low computation time.

Different solutions for modeling issues have been proposed in the literature. A survey on models for nonlinear inductors has been recently published [7]. Two different approaches are possible: the "external" or "behavioral" representation and the "physical" model in which each component of the model has a correspondence with a physical phenomenon. It is noteworthy that [7] addresses power electronics applications and takes into consideration behavioral models giving the representation of the inductor by the inductance versus current relationship (eventually including temperature as a parameter). Among the behavioral models, two analytical approaches have been proposed in the literature; they are both based on mathematical functions with a shape similar to the curve of the inductance to be reproduced. The first model, named the arctan model, uses the arctangent curve to retrieve a model of the inductor in bidirectional DC/DC converters [8], or in general for DC/DC converter applications [11,12]; differently, the latter exploits a third-order polynomial [18]. Both models consider the temperature [19–21]. This parameter is crucial; indeed, in the nonlinear zone, the inductance shows a variation with the current. Both the temperature and the current affect the inductance in steady state [22], and in dynamic conditions [23,24]; in addition, when operated near saturation, the inductor temperature increases, and its peak is enhanced, potentially leading to thermal runaway [19]. Both models are able to reproduce the inductance curve up to saturation with different performances. The polynomial model better reproduces the slight increase in the inductance for small currents; however, after the deep saturation point, it does not reproduce the asymptotic behavior. Instead, the arctan model shows a slightly decreasing trend for small currents, and this deep saturation behavior is better reproduced for higher currents (even if the asymptote is reached when the current tends to infinity). This feature is helpful in the simulation when high current peaks can be reached; instead, the inductance calculation employing the polynomial model from the point of view of the computation time is faster [22]. The literature considered the use of neural networks to design inductors [25,26]; an application to the design of power inductors is given by, [27] that exploits a hybrid method, which combines the accuracy of the 3D finite element method (FEM) and the low computational cost of artificial neural networks (ANNs) to optimize an inductor for a 2 kW converter. Neural networks were applied in [28] to retrieve loss maps for inductors and transformers. In contrast, [29] is focused on the same issue as is considered here; however, it employs a feedforward neural model to represent the behavior of power inductors. The network proposed by [29] is relatively simple, but the learning is performed only at environmental temperature. No other relevant contributions dealing with inductor modeling by neural networks are given in literature.

This paper presents the application of a well-established feedforward neural architecture with automatic learning of the activation functions of its hidden units. The architecture was first proposed in [30], and it has since been optimized [31,32], and successfully applied in challenging applications, such as speech recognition [33], In this paper a hybrid approach based on the neural net and the traditional interpolation approach is performed to optimize the computational effort. The αNet trained on a suitable dataset is able to reproduce any value of the inductance for a given current and temperature in the whole operating range.

Concerning the motivation of this paper: it seeks to advance studies on the dynamics of nonlinear systems by proposing an inductor model that is based on a neural network. Our approach aims to model the curves that are representative of the inductance behaviour, including saturation and temperature. Accordingly, the αNet network is optimized for curves (in the inductance vs. current plane) that start at a nonzero initial level (called the nominal value at zero current) and then decrease, showing asymptotic behavior at saturation. This is the underlying working hypothesis. The novelty of this paper consists of devising the αNet neural network and using it to model a nonlinear inductor including the

temperature as a parameter. This enhanced model is named E-αNet. Besides, instead of learning a surface in the three-dimensional space, the learning phase is based on 2-dimensional curves with the temperature as a parameter. The production exploits a weighted interpolation to retrieve intermediate points. This hybrid approach makes the E-αNet operation straightforward.

The proposed architecture E-αNet exploits Hermite's polynomials, allowing a smoothed curve with a reduced number of neurons. To the authors' knowledge, no similar approach has been presented until now, and this study presents the first model based on a neural network that considers temperature; consequently, this is the main contribution of the paper.

The remainder of this paper is organized as follows: Sect. 2 explains the problem definition and the main motivation of this work, Sect. 3 presents the αNET network, and Sect. 4 describes the nonlinear behavior of an inductor when it is operated up to saturation and presents the two inductors under study. The training set is described in Sect. 5, and the results are given in Sect. 6, where the current flowing through two inductors in different operating conditions is compared to the one experimentally obtained, including a comparison with the two main models proposed in the literature.

2 Problem definition and motivation

This paper aims to contribute to the field of modeling nonlinear curves and related applications to compute a parameter that varies dynamically with such curves. We chose to model the nonlinear behavior of an inductor as a function of the current flowing through it because this scenario is of practical interest in the design of DC/DC converters. These converters exploit the inductor as a reservoir of energy that is charged and discharged depending on the applied voltage. Because current flowing in an inductor indicates an increase in temperature, the expected result is a model of the inductor with temperature as a parameter. Two analytical models capable of representing inductance as a function of temperature have been proposed in the literature: the polynomial model and the model based on the arctangent trigonometric function known as the arctan model. Both models fit a curve with a trend that reproduces the typical trend of a nonlinear inductor. The polynomial model better reproduces the slight increase in the inductance for small currents; however, it does not reproduce the asymptotic behavior after the deep saturation point. Instead, the arctan model shows a slightly decreasing trend for small currents, and the deep saturation behavior is better reproduced for higher currents (even if the asymptote is reached when the current tends to be infinite). Figure 1 shows a comparison between the experimental data and the curves obtained with the polynomial and arctan models.

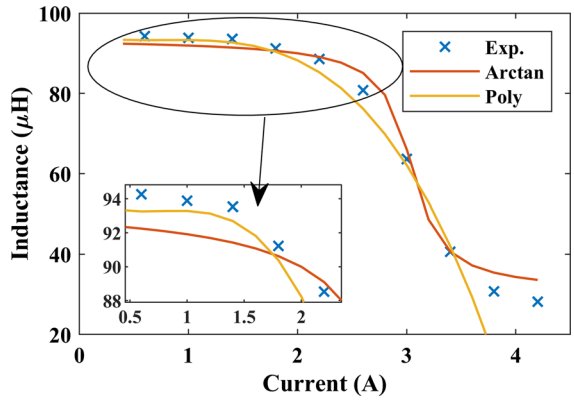

Fig. 1 comparison of experimental points and the curves obtained by polynomial and arctan models: the zoom shows that for small current, the polynomial model gives a better accuracy, whereas the arctan model suitably reproduces the asymptote

Minimizing the error between the model and the actual behavior is essential, especially when iterative algorithms are used. For example, calculating the current flowing through the inductor includes discretizing the constitutive equation, where V is the voltage applied to the inductor, i is the current flowing through it, T is the core temperature which can be considered constant during a switching period and T_s is the time interval or sampling time:

$$V = L(i, T)\frac{di}{dt} \tag{1}$$

yields:

$$i_{k+1} = VT_s\frac{1}{L(i_k, T)} + i_k \tag{2}$$

Then, the value at time k+1 is given by the value at time k plus a quantity provided by the ratio of the voltage multiplied by the sampling period to the value of the inductance. The error is given by:

$$\Delta i_{k+1} = \frac{\delta}{\delta L}\left(VT_s \frac{1}{L(i_k, T)}\right)\Delta L + \Delta i_k \tag{3}$$

For each iteration, due to the error propagation, a quantity that is proportional to the error on the inductance is added; therefore, the model must be accurate to avoid an overestimation of the maximum current. The most critical parameters to calculate the accuracy of the modeling are the maximum value of the estimated current and the root mean square error. The first parameter is crucial for designing the circuit in which the inductor is employed; in fact, knowledge of the maximum current is essential to design the main components of the same circuit. The RMS error allows the curves obtained by different models to be compared. We proposed a new approach based on a neural network because in general, neural networks show better performance in approximating curves. On the other hand, both the learning and production phases can be cumbersome; we solved these issues by learning five 2-dimensional curves with the temperature as a parameter instead of training on a surface in the 3-dimensional space defined by the core temperature, current, and inductance. In addition, the production exploits the interpolation described by Eq. (16) to retrieve the intermediate points whose temperature does not belong to the trained curves. The main motivation for this work is to obtain a more accurate model than those proposed thus far in the literature. Such a model is able to provide the value of inductance as a function of current and temperature, and can be exploited for calculating the current.

3 The EαNet neural network

In this section, an enhanced version of the feed-forward architecture previously developed in [31] (αNet) is reported. The αNet architecture is a shallow feedforward neural network that can modify the activation function of its hidden units using the Hermite regression formula and the conjugate gradient descent algorithm [34].

The αNet architecture has been successfully applied to address regression tasks, outperforming traditional MLP architectures using sigmoidal or sinusoidal activation functions. Notably, it has shown very good performances in various benchmark problems, including the Add-10 Regression problem proposed by J. Friedman [35], the 5-parity problem [36], and the Two Spirals benchmark [37]. In each case, αNet has been employed to tackle these challenges as regression problems, demonstrating its better effectiveness than conventional feed-forward neural architectures [31].

The enhanced version, which has also been used in different contexts [30,33], also optimizes the number of Hermite polynomials for each hidden unit with a pruning algorithm that cuts off unnecessary Hermite coefficients. The pruning algorithm performs a sensitivity analysis of the error of approximation calculated in the training points concerning each Hermite expansion coefficient [30].

3.1 Background: quality factors

The authors of [31,32] have previously introduced three "quality factors" to provide an *a-priori* measure of the generalization capability of a shallow feed-forward neural network without shortcut with I inputs, O outputs and H hidden units.

Learning Quality Factor $\mathbf{Q_L}$: let K be the number elements belonging to the training set, O be the number of output units, $t_i^{(j)}$ be the i-th component of the j-th training pattern, and $o_i^{(j)}$ be the i-th component of the j-th output desired pattern. Then, the *Learning Quality Factor* is defined as:

$$Q_L = \frac{1}{K}\sum_{j=0}^{K-1}\sum_{i=0}^{O-1}\left(t_i^{(j)} - o_i^{(j)}\right)^2 \tag{4}$$

This quality factor estimates the network's learning ability over the training set, being simply the RMS error computed on the Training Set samples.

Generalization Quality Factor $\mathbf{Q_G}$: let K be the number of training set items, O be the number of output units, $\mathbf{t}_j$ be the j-th training item, and $|\nabla \mathbf{u}_i|^2_{\mathbf{t}_j}$ be the squared modulus of the network i-th output unit gradient when the input item is $\mathbf{t}_j$. Then, the *generalization quality factor* is defined as:

$$Q_G = \frac{1}{K}\sum_{j=0}^{K-1}\sum_{i=0}^{O-1}|\nabla \mathbf{u}_i|^2_{\mathbf{t}_j} \tag{5}$$

This quality factor computes the gradient of the network output function in the training points thus evaluating *,a priori,* the network's generalization capability.

Production Cost Quality Factor $\mathbf{Q_P}$: The *production cost quality factor* is defined as:

$$Q_P = H \cdot (I + O) \tag{6}$$

It assesses the computational cost of the network during the production phase, measured by the quantity of connections among the network units.

3.2 The E-αNet architecture

The E-αNet is an advanced version of the αNet feed-forward neural architecture [31]. The αNet has the ability to learn the activation function of its hidden units while training, leading to significantly lower values of both Q_G and Q_P quality factors compared to a conventional feed-forward network using sigmoidal activation functions for its hidden units [31]. This feature is achieved through the joint use of the CGD optimization algorithm with the Powell restart conditions [34], and the Hermite regression formula. The Hermite regression employs the first R Hermite orthonormal functions to represent the activation function of each hidden unit. The E-αNet has the feature of selecting the most relevant Hermite orthonormal functions for each hidden unit, thereby enhancing the network's performance [30,33].

The E-αNet architecture closely resembles a typical shallow three-layered feed-forward network. While the output layer units use linear activation functions, the hidden layer units in E-αNet have a unique structure, relying on Hermite orthonormal functions for function approximation.

As a matter of fact, let R be the number of the first Hermite orthonormal functions used to approximate the activation function of the k-th hidden unit. Let $h_{rk}\,(x)$ be the r-th Hermite orthonormal function belonging to the k-th hidden unit. In particular, let H_r be the r-th orthogonal Hermite polynomial, and let $\Phi(x)$ be a Gaussian function with zero mean and unitary variance. The r-th Hermite orthonormal function expression is:

$$h_r(x) = r!^{-\frac{1}{2}} \cdot \pi^{\frac{1}{4}} \cdot 2^{-\frac{r-1}{2}} \cdot H_r(x) \cdot \Phi(x) \tag{7}$$

with $-\infty < x < +\infty$. The k-th hidden unit of the E-αNet architecture is provided with an activation function $f_k^*\,(x)$ given by:

$$f_k^*\,(x) = \sum_{r=1}^{R} c_{rk}^* h_{rk}\,(x) \tag{8}$$

The choice of this approximation function aims to yield a continuous, smooth, representation of the output function for any unit in the output layer. Additionally, Hermite polynomials can be recursively and easily computed, including their first derivatives [38]:

$$\frac{d}{dx} f^*(x) = \sum_{r=1}^{R} ((2r)^{\frac{1}{2}} h_{r-1}(x) - x h_r(x)) \tag{9}$$

In E-αNet, the number R of Hermite orthonormal functions of each hidden units dynamically adapts through a pruning algorithm. This algorithm leverages information about the sensitivity of the Q_E factor to each weight within the Hermite functions associated with hidden units. This configuration results in a highly adaptable neural architecture with strong generalization capabilities [30,39].

Figure 2 shows the typical unit belonging to the hidden layer of E-αNet: the dashed square represents the activation function block. The architecture of the αNet unit reflects the Eq. (8) formula. The weights c_{rk}^* of each unit belonging to the hidden layer will be learned during the training phase.

3.3 E-αNet learning

The learning algorithm effectively combines the Hermite regression formula with the conjugate gradient descent (CGRD) algorithm, incorporating Powell's restart conditions. It further integrates sensitivity analysis regarding the factor Q_E concerning the weights c_{rk}^*. This analysis optimizes the quantity of orthonormal Hermite functions required by each hidden unit to represent its activation function.

During the training phase, the coefficients c_{rk}^* for each hidden artificial neuron and the weights of connections between αNet units are jointly adjusted using the CGRD algorithm with Powell's restart conditions [34]. This continuous adjustment of the activation functions for each hidden unit persists until the minimum training set error is achieved [31,32].

In E-αNet, the initial training phase sets a maximum limit of R as R_{max}, followed by the application of a pruning algorithm. This algorithm effectively reduces

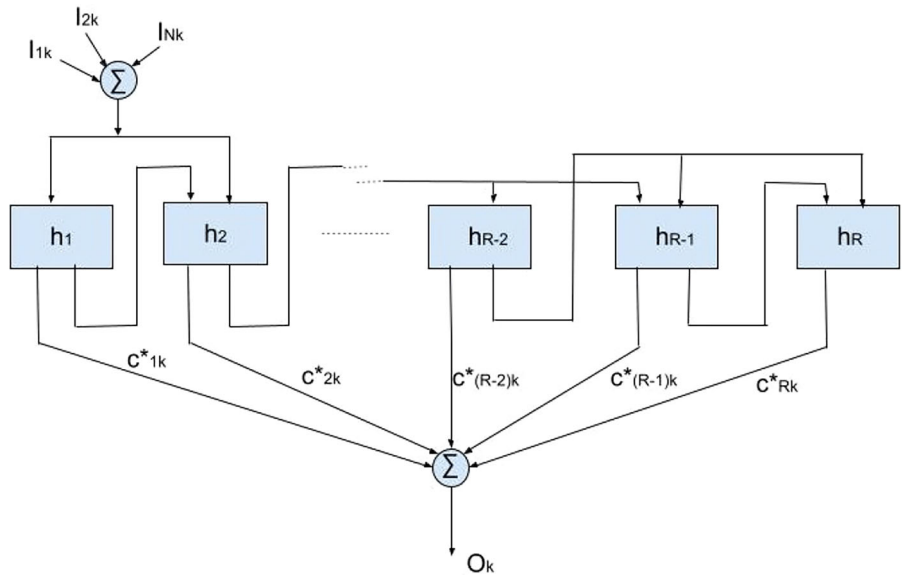

Fig. 2 The EαNet hidden unit

the number of Hermite orthonormal functions required to describe and calculate each hidden unit's activation function independently [39].

The pruning algorithm operates on the premise of eliminating coefficients that demonstrate lower relevance based on a specified network behavior criterion. Relevance is quantified using error sensitivity [40].

To assess the feasibility of pruning the r-th connection of the k-th hidden unit in E-αNet, it is essential to investigate the sensitivity of the training error quality factor Q_E concerning the weight c^*_{rk}.

Let $Q_{E\setminus c^*_{rk}}$ be the value of the learning quality factor without considering the weight c^*_{rk}; then, the sensitivity of the Q_E factor with respect to the weight c^*_{rk}, $S_{rk}\left(c^*_{rk}\right)$, is defined as:

$$S_{rk}\left(c^*_{rk}\right) = \left| Q_{E\setminus c^*_{rk}} - Q_E \right| \tag{10}$$

Equation (10) can also be written as:

$$S_{rk}\left(c^*_{rk}\right) = \left| \frac{\partial Q_E}{\partial c^*_{rk}} \cdot c^*_{rk} \right| \tag{11}$$

Therefore, it is necessary to compute all the sensitivities $S_{rk}\left(c^*_{rk}\right)$ to identify the unnecessary c^*_{rk}, i.e., to determine the weights c^*_{rk} that do not significantly affect the final value of Q_E. The whole learning procedure of E-αNet can be described in the following steps:

1. Initialization
2. Weights learning
3. Pruning of the unnecessary c^*_{rk} connections
4. End Test

In the following paragraphs, all the steps are illustrated in detail.

Initialization In this phase, the network's topology is determined, including the number of inputs I, outputs O, and hidden units H. Subsequently, all connection weights between the $I + H + O$ network units are randomly initialized. Furthermore, the other two parameters are fixed in advance:

- The starting number R_{max} of the Hermite orthonormal functions needed by each hidden unit of αNet to model its own activation function.
  In this starting phase, the R_{max} coefficients of each hidden unit are chosen so that they can Model a Gaussian function.
- A threshold $T_{S_{min}} \in [0, 1]$: this threshold is used for the pruning of the unnecessary weights c^*_{rk} of the hidden units of αNet

Weights learning During this training phase, the coefficients c^*_{rk} are changed together with the weights of the connections between the units of αNet using the CGRD algorithm with Powell's restart conditions [34]; hence, each activation function of each hidden unit of αNet is continuously changed until the minimum of Q_E is reached.

The use of the conjugate gradient descent optimization algorithm with the restart conditions of Powell is due to its high computational speed, its optimal performances for high-grade polynomial functions, and

the reasonable amount of memory needed, where the amount increases linearly with the number of variables. The utilization of both the CGRD algorithm and the Hermite regression formula results in reduced Q_G and Q_P values, thereby enhancing the neural architecture's generalization capacity and lowering computational costs in the production phase, compared to a conventional feed-forward architecture employing sigmoid activation functions for its hidden units [31,32].

Pruning Algorithm After, the learning period is over, and all the sensitivities $S_{rk}\left(c_{rk}^{*}\right)$ are calculated. Then, for each hidden unit, the sensitivities $S_{rk}\left(c_{rk}^{*}\right)$ are normalized between 0 and 1. Subsequently, those weights whose corresponding sensitivities satisfy the following inequality:

$$S_{rk}\left(c_{rk}^{*}\right) < T_{S_{min}} \tag{12}$$

are disregarded and they will no longer be considered in the learning process, since, if inequality (12) is satisfied, the weight c_{rk}^{*} does not affect the final value of Q_E.

End Test In this phase, a test is conducted: if in the previous step there was at least one c_{rk}^{*} connection cut off, then the learning algorithm will be repeated from step 2, considering all the connection weights between the $I + H + O$ units of the network and all the weights c_{rk}^{*} that did not satisfy the inequality (12). If none of the c_{rk}^{*} parameters was disregarded in the previous step, the training process is over.

4 Fundamentals on nonlinear inductors

4.1 Behavior of a nonlinear inductor

An inductor is characterized by a differential equation in which the voltage at its terminal is proportional to the current derivative. In a linear inductor, the inductance is constant; it is described by Eq. (13).

$$V = L\frac{di}{dt} \tag{13}$$

The nonlinear behavior is characterized by an inductance value that depends on the current and the temperature T, as in Eq. (14):

$$V = L_{diff}(i, T)\frac{di}{dt} \tag{14}$$

In this case, the differential inductance must be considered since the slope of the curve described by the magnetic flux vs. the current varies (contrary to a linear inductor in which the slope is constant), as shown in Fig. 3. The differential inductance is the slope of the total flux linkage Φ as a function of the magnetizing current [8]. All inductors adopting a magnetic core are characterized by a nonlinear behavior: the inductance exhibited at small current decreases when the current increases, then it tends asymptotically to a constant value representing the deep saturation. This characteristic is common to any power inductor since they exhibits the same profile with a different scale factor [41] The traditional approach considers a current range in which the inductance remains constant; for this reason, the inductor is also named a linear inductor. Increasing the current beyond the linear zone, the decrease in the inductance is appreciable. When a constant voltage is applied to the linear inductor, its current is linear. In contrast, in the case of a nonlinear inductor, the current shape differs, showing a cusp. In addition, a nonlinear inductor shows a lower minimum current and a higher maximum compared to a linear inductor. These aspects have practical implications because, in switched mode power supplies, the current peak also stresses the power switch and affects the reliability of the circuit. For this reason, a proper model is needed to perform the analysis, particularly to reproduce the current shape. Usually, inductors' manufacturers give the rated value of the inductance. This inductance is typically assumed constant up to the rated current, with a maximum decrease of 10%. As a consequence, to retrieve the inductance vs. current curve, describing the nonlinearity, laboratory testing should be done [18,42–45]. The magnetic behavior of the inductor depends on the core material. Ferrite is widely used in power electronics applications since it exhibits low losses and high resistivity in a broad frequency spectrum. In addition, the Curie temperature is approximately 700 °C, and the magnetic properties are isotropic. The saturation induction ranges from 0.25 T to 0.45 T, while the relative permeability ranges from 1×10^3 to 20×10^3 [13].

Two inductors have been considered in this paper, and they have been characterized by a dedicated measurement system [18,42,43]. This system imposes two different voltage values on the inductor so that it is charged and discharged across a load. Consequently, the inductor is subjected to a current composed of a DC part and a superimposed AC component. The current slope is calculated based on a least squares regression performed on a set of 50 samples at a time. This

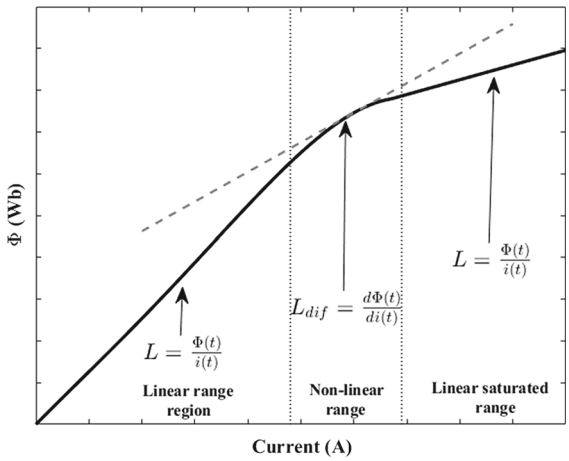

Fig. 3 Typical magnetization characteristic of a core made of ferrite

value of the differential inductance is associated with the mean value of the current calculated on the same samples, obtaining a vector with the inductance values versus the current as in Eq. (15), where V_L is the voltage applied across the inductors' terminals. This is the actual voltage applied to the inductor obtained from that measured by excluding drops due to losses, as explained in [19]. During the measurement, the core temperature T is also acquired so that each inductance point is associated with the corresponding temperature.

$$L_{diff}(i, T) = \frac{V_L}{\frac{di}{dt}} \tag{15}$$

4.2 The inductors under study

The two inductors studied here are the model DO 5010H 334[1] and the model DO 5010H 104,[2] as provided by Coilcraft. They are both ferrite inductors wound on the same core with a different number of turns to obtain a different value of inductance and of the maximum operating current. The inductor DO 5010H 104 has a rated value of 100 μH and a maximum current of 3 A. The inductor DO 5010H 334 has a rated value of 330 μH and a maximum current of 1.9 A. These values of the maximum current, given by the manufacturer,

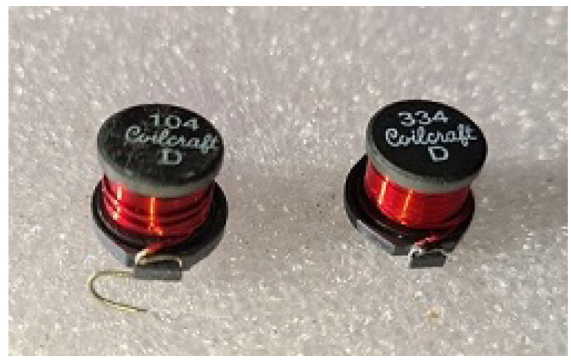

Fig. 4 The two inductors under study

correspond to a decrease of 10% of the inductance. The manufacturer indicates this value as "saturation"; however, we adopt this term for a current corresponding to one half of the rated value of the inductance to extend the operating range. Figure 4 shows the two inductors.

5 The training dataset

The training dataset works with a reduced set of points because they have to be measured directly on the component under study. Each point gives the differential inductance versus the current at a defined temperature. The measurement system is described in detail in [18,42,43]. This system is devised to impose a constant voltage on the inductor under test and to measure the current slope indicated as V_L and di/dt in Eq. (15), respectively. For a given temperature, some points representing the inductance versus the current are measured according to Eq. (15). Only five temperatures were considered for training, starting from the environmental temperature to the maximum allowed, aiming to obtain five curves by the E-αNet. As explained above, in this way, the network is simpler, allowing a faster learning phase.

Each feature has been normalized to a specified range using the "MinMaxScaler"[3] [46] procedure for computational purposes. This procedure linearly transforms the feature values to fit within a fixed range, where the highest data point corresponds to the maximum value and the lowest data point corresponds to the minimum value. In particular, each feature in the

[1] https://www.coilcraft.com/en-us/products/power/unshielded-inductors/ferrite-drum-surface-mount/do/do5010h/do5010h-334/.

[2] https://www.coilcraft.com/en-us/products/power/unshielded-inductors/ferrite-drum-surface-mount/do/do5010h/do5010h-104/.

[3] https://scikit-learn.org/stable/modules/generated/sklearn.preprocessing.MinMaxScaler.html.

measurement dataset has been individually scaled to the real interval [0.0, 1.0].

After training the neural network, the scaling parameters are applied to the test set data, which are provided as inputs to the network to obtain the desired outcomes. The results are then inversely transformed to get the correct, physically meaningful values in the desired units of measurement.

Since the transformation process is linear, it does not distort the inputs or outcomes. Moreover, the learning process remains the same, it does not depend of the numeric values given by different measures, provided in the dataset, which may vary according to the specific inductor component whose characteristics must be modeled; i.e. the transformation procedure is transparent to the learning process.

For a given current, the points belonging to temperatures different from the training set are calculated according to:

$$L(T_x) = L_2 \frac{(T_x - T_1)}{(T_2 - T1)} + L_1 \frac{(T_2 - T_x)}{(T_2 - T1)} \tag{16}$$

with

$$T_1 < T_x < T_2 \tag{17}$$

where L_x is the needed inductance corresponding to the temperature T_x and T_1 and T_2 are the temperatures corresponding to the closest temperatures given by the learned curves. This allows us to more closely weight the nearest temperature. Characterization was performed for the two inductors, namely, the model DO 5010H 334 and the model DO 5010H-104.

5.1 Characterization of inductor DO 5010H-104

The representative points used for training the neural network are shown in Fig. 5. It can be noted that only five temperatures were considered (25 °C, 45 °C, 65 °C, 85 °C, 105 °C), and for each temperature, 18 points, inductance vs. current, were used. The curves obtained by the E-αNet are shown in Fig. 5. They encompass the dataset points, as expected, and are able to describe the inductor's behavior from low currents up to saturation. The architecture that has been used for E-αNet is characterized by one input unit, one output unit and two hidden units, each one with a maximum of 14 Hermite polynomials. The slope of the linear output unit is 0.4.

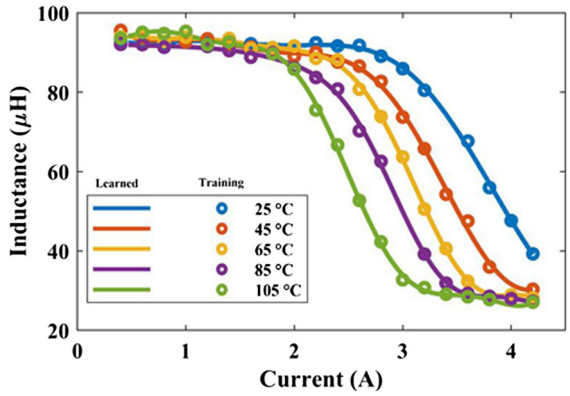

Fig. 5 Training set and learned curves for inductor 104

5.2 Characterization of the inductor DO 5010H-334

The representative points adopted for training inductor DO 5010H-104 and the learned curves obtained by E-αNet are shown in Fig. 6. The architecture that has been used for E-αNet is characterized by one input unit, one output unit and one hidden unit with a maximum of 9 Hermite polynomials. The slope of the linear output unit is 0.4. Additionally, in this case, five temperatures were considered with 18 pairs of inductance vs. current for each temperature. They encompass the dataset points, as expected, and are able to describe the inductor's behavior from low currents up to deep saturation. For both inductors, the rated inductance given by the manufacturer is retrieved at low currents, and this inductance does not depend on the temperature, as shown by the superposition of the curves. In contrast, for higher currents, the inductance values change as a function of the temperature up to deep saturation, where the inductance is again constant, albeit with a drastically reduced value.

6 Results

An indirect method was used to verify the accuracy of fit of the proposed approach. Particularly, the correspondence of the value of the inductance modeled by the E-αNet network with the true value has been verified by calculating the current flowing through the inductor and comparing it with that measured at the same applied voltage. This approach complies with practical applications in which the knowledge of the current flowing through an inductor is crucial. Toward

Table 1 Test conditions and errors for the inductor DO 5010H 104

Temp [°C]	V_L [V]	T_{ON} [µs]	n	RMSE [A]	%Err on max
40	24	12.5	72	0.058	0.69
60	24	12.5	72	0.0097	0.74
75	24	12.5	72	0.011	1.48
80	24	12.5	72	0.016	-1.89

Table 2 Test conditions and errors for the inductor DO 5010H 334

Temp [°C]	V_L [V]	T_{ON} [µs]	n	RMSE [A]	%Err on max
40	24	12.5	57	0.0023	−0.33
60	24	12.5	55	0.0015	−0.58
75	24	12.5	54	0.0052	−0.15
80	24	12.5	53	0.0084	−0.39

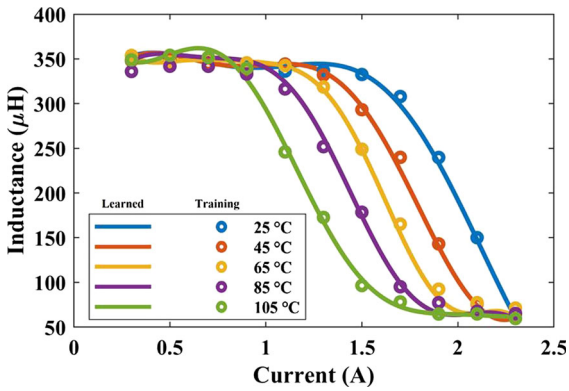

Fig. 6 Training set and learned curves for inductor 334

this end, Eq. (14) was solved numerically over a time interval in which a constant voltage V_L is applied to the inductor.

$$i_L(k+1) = i_L(k) + \frac{V_L \Delta T}{L(i_L(k))} \tag{18}$$

From Eq. (18), a vector containing the current versus time is obtained. The experimental tests were carried out on both inductors modeled by the proposed neural network. In testing, the current profiles obtained by Eq. (18) for a given temperature are compared with the experimental values sampled on a power switching converter employing these inductors. The inductor is subjected to a constant voltage V_L applied for a constant time interval $T_{ON} = n\Delta$T, where n represents the number of samples. For each inductor, the main parameters adopted for the tests are summarized in Tables 1 and 2. In the same tables, the percent error calculated on the maximum current and the root mean square error (RMSE) and as in Eqs. (19) and (20), are given. The percent error is of practical importance because the maximum current is a design parameter. We defined the error with its sign to emphasize that when the calculated current is greater than the corresponding experimental value (overestimation of the maximum), the error gives a negative value, whereas an underestimation corresponds to a positive value. The RMSE is useful for analyzing the correspondence between the experimental and calculated curves during the whole switching period. A more accurate estimation of the current shape allows precise knowledge of its spectrum and a proper filter design [47].

$$\%error = \frac{i_{exp(max)} - i_{calc(max)}}{i_{exp(max)}} 100 \tag{19}$$

$$RMSE = \frac{\sqrt{\Sigma (i_{exp} - i_{meas})^2}}{n} \tag{20}$$

6.1 Analysis of the current for inductor DO 5010H-104

The current flowing through the inductor DO 5010H-104 was calculated at four different temperatures according to the test conditions summarized in Table 1. A constant voltage of 24 V is applied to the inductor, and it is maintained for 12.5 µs; the current is calculated as in Eq. (18). The time interval of 12.5 µs is constant

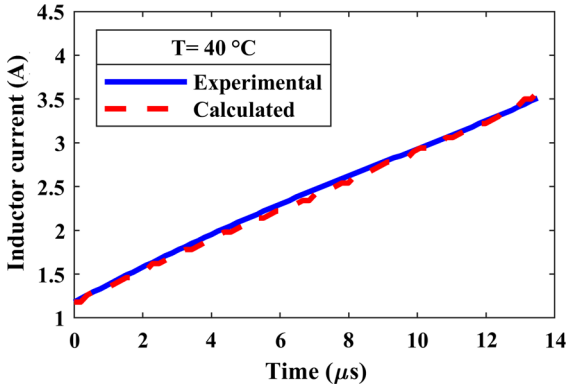

Fig. 7 Current profile comparison for inductor 104 at T=40 °C

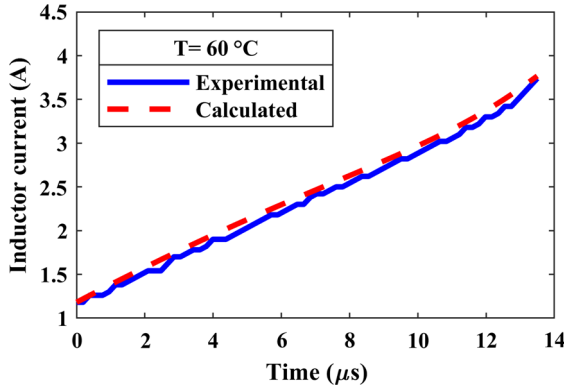

Fig. 8 Current profile comparison for inductor 104 at T=60 °C

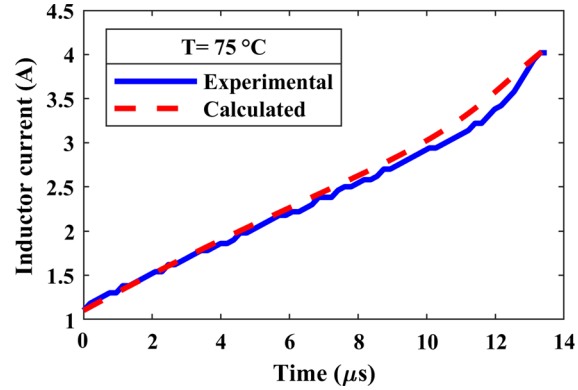

Fig. 9 Current profile comparison for the inductor 104 at T=75 °C

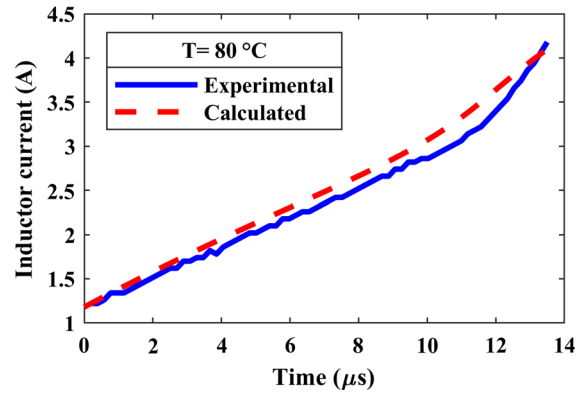

Fig. 10 Current profile comparison for inductor 104 at T=80 °C

to demonstrate the influence of temperature. Initially, the current always grows linearly; nonlinearity occurs after current increases, and this nonlinearity becomes more pronounced at higher temperatures. Such behavior is common for all inductors wound on ferromagnetic cores. The values or the current calculated by the neural model versus time are compared with the experimental values in Figs. 7, 8, 9 and 10 for T=40 °C, T=60 °C, T=75 °C and T=80 °C, respectively. The experimental curves can be readily overlaid with those obtained by the neural model, which shows that the maxima do not differ significantly. Considering the RMSE and the percent error given in Table 1, in the worst condition, the RMSE is equal to 0.058 A, and the percent error on the maximum value of the current is 1.89%. The higher temperature represents the worst case because a slight deviation of the curves is recognizable for higher currents. It is valuable to note that the error is always less than 2%.

6.2 Analysis of the current for the inductor DO 5010H 334

The current flowing through the inductor DO 5010H-334 was calculated at four different temperatures according to the test conditions summarized in Table 2. In this case, a constant voltage of 24 V is applied to the inductor, and it is maintained for 12.5 μs. Because the inductance is higher than that in the previous test, lower currents are obtained; however, the same behavior is observed: the current starts growing linearly, and the nonlinearity is recognizable at higher currents and is more evident at higher temperatures. The values or the current calculated by the neural model versus time are compared with the experimental values in Figs. 11, 12, 13 and 14 for T=40 °C, T=60 °C, T=75 °C and T=80 °C, respectively. Additionally, in this case, a consistent overlay with the current obtained by the neu-

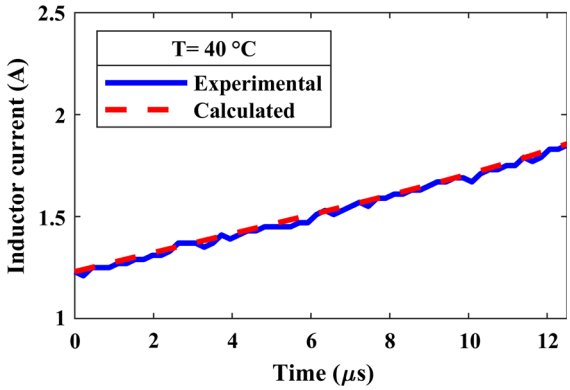

Fig. 11 Current profile comparison for inductor 334 at T=40 °C

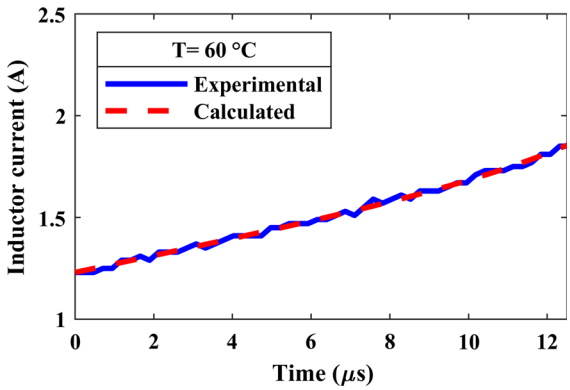

Fig. 12 Current profile comparison for inductor 334 at T=60 °C

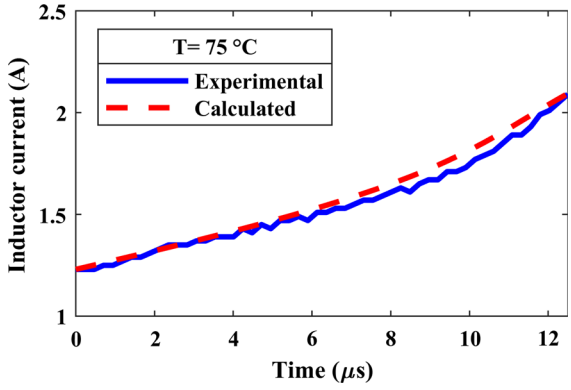

Fig. 13 Current profile comparison for inductor 334 at T=75 °C

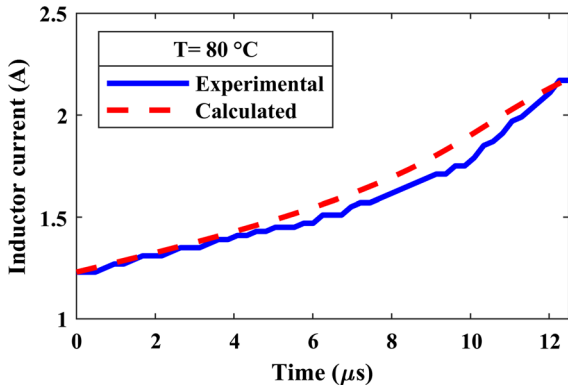

Fig. 14 Current profile comparison for inductor 334 at T=80 °C

ral model is observed, and the maxima of both practically coincide. Considering the RMSE and the % error given in Table 2, in the worst condition, the RMSE is equal to 0.084 A, and the percent error on the maximum value of the current is −0.58%. It is valuable to note that the error is always less than 1%.

6.3 Comparison with the analytical models proposed in the literature

In this section, the results obtained by the E-αNet-based models are compared with the two main models proposed in the literature: the arctan and the polynomial models. Both models were implemented following the methods described by their authors and summarized in [22]. An example on the performance of the models is summarized in Fig. 15 which shows the ability of the E-αNet in following more accurately the experimental points with respect to the other models. In fact, both low current and deep saturation regions are well approximated. The comparison is performed for both tested inductors considering the curves in which the highest current is reached since it represents the worst case. The comparison of the four current profiles obtained by the neural model, the polynomial and arctan model with the experimental data is represented in Figs. 16 and 17, for inductors 104 and 334, respectively. Notably, all curves reproduce the nonlinear effect on current; however, the proposed neural model shows a better accuracy concerning both the shape and the maximum value. The errors in terms of percent on the maximum and RMSE are summarized by bar diagrams in Figs. 18, 19, 20 and 21, respectively. A smaller bar corresponds to a lower error and therefore to better modeling. The figures facilitate comparison of the error calculated based on the experimental data, based on the currents calculated by the proposed neural model and based on

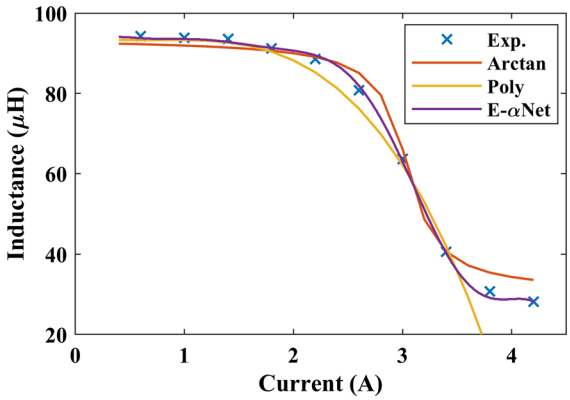

Fig. 15 Inductance profile comparison for inductor 104 with analytical models at T=65 °C

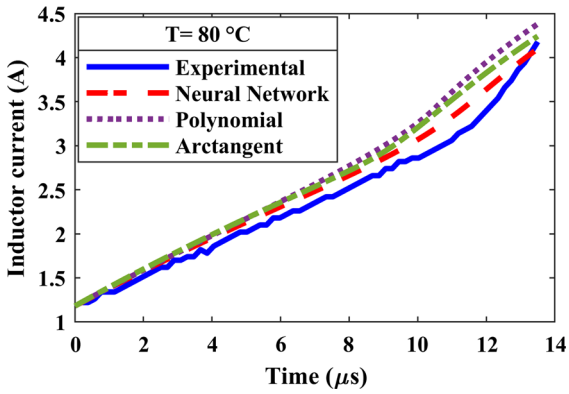

Fig. 16 Comparison of the experimental profile of inductor 104 with analytical models at T=80 °C

the currents calculated by two analytical models taken from literature. Notably, the proposed neural networks provide a better approximation of the current by showing lower error values both in terms of RMSE and on the maximum current.

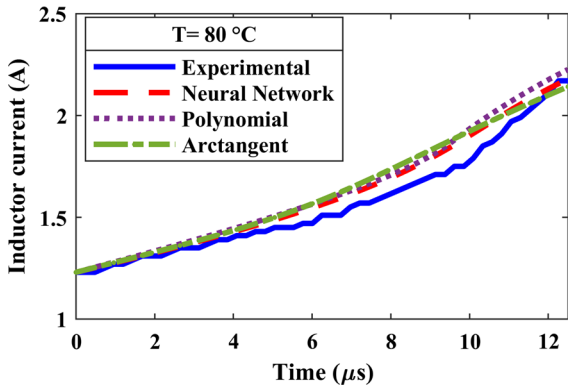

Fig. 17 Comparison of the experimental profile of inductor 334 with analytical models at T=80 °C

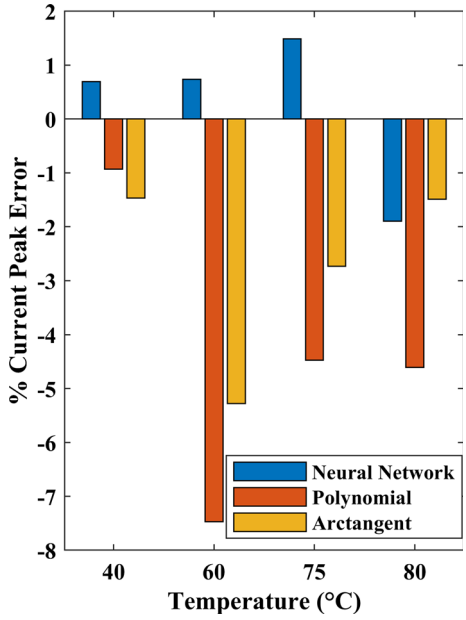

Fig. 18 Percent error on the maximum current obtained with the neural, polynomial and arctan model for the inductor 104 at T=80 °C

7 Conclusions

A neural network, E-αNet, has been devised to retrieve the model of nonlinear power inductors; the proposed approach combines the features of the E-αNet with classical weighted interpolation permitting accurate modeling of both the learning and production phases. In fact, the learning phase exploits five 2-dimensional curves and avoids learning a 3-dimensional surface. The proposed architecture E-αNet exploits Hermite's polynomials, realizing a smoothed curve with a reduced number of neurons. The production uses a traditional weighted interpolation to retrieve the intermediate points. This work represents the first time that modeling by a neural network includes consideration of the temperature of the magnetic core. E-αNet revealed suitable for this purpose since, on the basis of a limited dataset for learning, it can learn representative curves of an inductor with temperature as a parameter. Verification of the proposed method has been performed in dynamic conditions by comparing the measured current flowing through two different inductors with those calculated

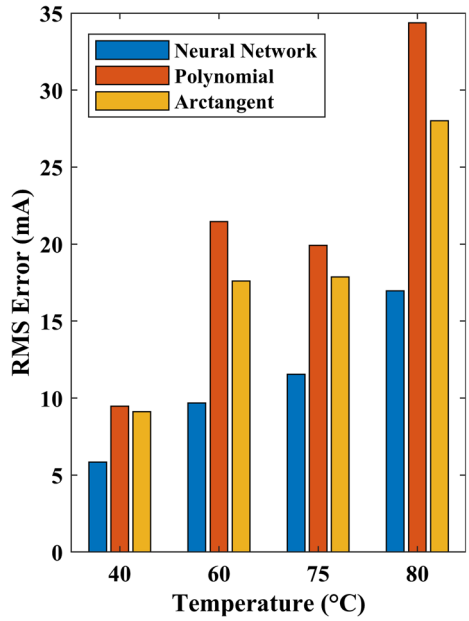

Fig. 19 RMSE obtained with the neural, polynomial and arctan models for inductor 104 at T=80 °C

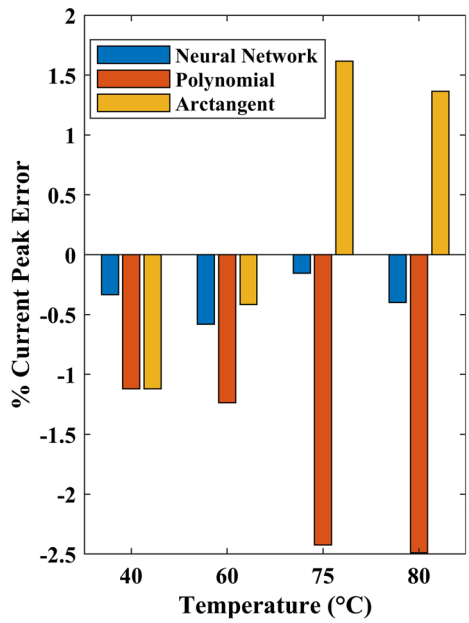

Fig. 20 Percent error on the maximum current obtained with the neural, polynomial and arctan models for inductor 334 at T=80 °C

by an existing neural model in several operating conditions. Results have been compared with those obtained by the two main analytical models proposed by the literature, considering the estimation of the maximum value

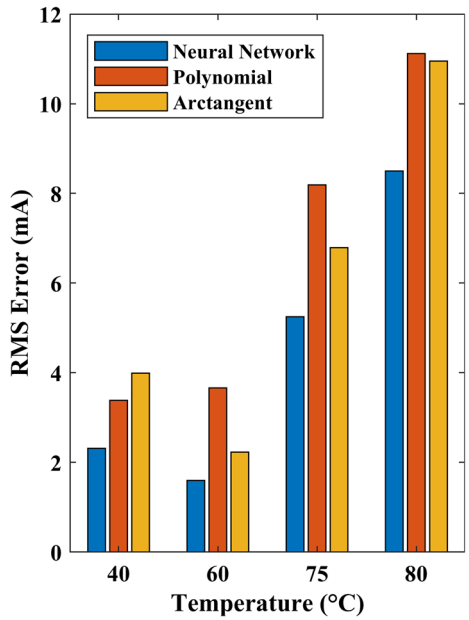

Fig. 21 RMSE obtained with the neural, polynomial and arctan models for inductor 334 at T=80 °C

of the current and the root mean squared error; in all cases, a lower error has been obtained, demonstrating the accuracy of the proposed approach. The proposed approach can be applied to all inductors wound on ferromagnetic cores; besides, this procedure is of practical interest in the design of switched mode power converters.

Author contributions All authors contributed equally to the present research work. All the authors have read and approved the final manuscript.

Funding Open access funding provided by Consiglio Nazionale Delle Ricerche (CNR) within the CRUI-CARE Agreement. This research was partially funded by the ECSEL-JU project REACTION (first and euRopEAn siC eigTh Inches pilOt liNe), Grant Agreement No. 783158.

Data availability The datasets generated and/or analyzed during the current study are available from the corresponding author upon reasonable request.

Declarations

Conflict of interest The authors have no relevant financial or nonfinancial interests to disclose.

8 Appendix

This appendix contains the pseudo code algorithms to retrieve the analytical models proposed by the literature based on experimental data measured on the inductor. Section 8.1 shows how to obtain the inductance curve by the arctan method. This approach is based on the shape of the arctan function suitably adapted to the inductance curve. The identification of this model is based on the knowledge of four coefficients: L_{nom}, $L_{30\%}$, $L_{70\%}$, and $L_{deepsat}$. L_{nom} is the nominal inductance of the inductor, and $L_{30\%}$ and $L_{70\%}$ correspond to the drops in the nominal inductance of 30% and 70% caused by two currents labeled $I_{30\%}$ and $I_{70\%}$, respectively. $L_{deepsat}$ is the inductance value in deep saturation. The Sect. 8.2 shows the pseudocode to calculate the inductance curve by the polynomial-based method. It exploits a third-order polynomial function. The polynomial model can be identified based on the same parameters: L_{nom}, $L_{30\%}$, $L_{70\%}$, and $L_{deepsat}$; however, better results can be retrieved by increasing the data. The coefficients of the polynomial are calculated by a least-squares regression (LSR). Finally, Sect. 8.3 describes the recursive algorithm to calculate the current as in Eq. (18). The algorithm can be executed based on the inductance curve retrieved by the arctan, polynomial or E-αNet network.

8.1 Arctan model

Pseudocode 1: Estimation algorithm for calculating the inductance through the arctangent model

```
%%INITIALIZATION
SET L_30;        %30%
   INDUCTANCE DROP TO THE
   NOMINAL VALUE
SET I_30;        %CURRENT AT
   WHICH INDUCTANCE DROP IS
   30% TO THE NOMINAL VALUE
SET L_70;        %70%
   INDUCTANCE DROP TO THE
   NOMINAL VALUE
SET I_70;        %CURRENT AT
   WHICH INDUCTANCE DROP IS
   70% TO THE NOMINAL VALUE
SET L_nom;       %NOMINAL
   INDUCTANCE
SET L_deepsat;   %INDUCTANCE
   VALUE FOR DEEP SATURATION

%%PARAMETER EVALUATION FOR THE
    ARCTANGENT INDUCTANCE
   MODEL
Gamma_30=(L_30-L_deepsat)/(
   L_nom-L_deepsat);
Gamma_70=(L_70-L_deepsat)/(
   L_nom-L_deepsat);
Sigma=(cot(pi*Gamma_30)-cot(pi
   *Gamma_70))/(I_30-I_70);
I_Lstar=(I_70*cot(pi*Gamma_30)
   -cot(pi*Gamma_70))/(cot(pi*
   Gamma_30)-cot(pi*Gamma_70))
   ;

%%ARCTANGENT MODEL OF THE
   INDUCTANCE AS A FUNCTION OF
    THE CURRENT "I"
L_arctan=L_deepsat+1/2*(L_nom-
   L_deepsat)*(1-2/pi*arctan(
   Sigma*(I-I_Lstar)));
```

8.2 Polynomial model

Pseudocode 2: Estimation algorithm for calculating the inductance through the polynomial model

```
%%INITIALIZATION
SET L_30;        %30%
   INDUCTANCE DROP TO THE
   NOMINAL VALUE
SET I_30;        %CURRENT AT
   WHICH INDUCTANCE DROP IS
   30% TO THE NOMINAL VALUE
```

```
SET L_70;        %70%
   INDUCTANCE DROP TO THE
   NOMINAL VALUE
SET I_70;        %CURRENT AT
   WHICH INDUCTANCE DROP IS
   70% TO THE NOMINAL VALUE
SET L_nom;       %NOMINAL
   INDUCTANCE
SET L_deepsat;   %INDUCTANCE
   VALUE FOR DEEP SATURATION
SET I_deepsat;   %CURRENT AT
   WHICH INDUCTANCE IS IN DEEP
    SATURATION
SET I_data;      %CURRENT RANGE
    FOR THE POLYNOMIAL
   REGRESSION

%%PARAMETER EVALUATION FOR THE
    POLYNOMIAL INDUCTANCE
   MODEL
[L_0,L_1,L_2,L_3]=polyfit(
   I_data,[0 L_nom;I_30 L_30;
   I_70 L_70;I_deepsat
Ldeepsat],3);     %LEAST-SQUARE
    REGRESSION TO ACHIEVE THE
   POLYNOMIAL FIT TO THE INPUT
    DATA

%%POLYNOMIAL MODEL OF THE
   INDUCTANCE AS A FUNCTION OF
    THE CURRENT "I"
L_poly=L_0+L_1*I+L_2*I^2+L_3*I
   ^3;
```

8.3 Current calculation

Pseudocode 3: Equation (18) discretization and calculation

```
%% CALCULATION OF THE CURRENT
   THROUGH THE INDUCTOR

SET Ton;                      %
   DEFINE ON TIME FOR THE
   MOSFET SWITCH
SET N;                        %
   DEFINE NUMBER OF STEPS FROM
    t=0 TO t=Ton
SET i_min;                    %
   DEFINE INITIAL CONDITION
   FOR THE CURRENT
SET INDUCTOR_MODEL;           %
   DEFINE WHICH MODEL USE TO
   EVALUATE THE INDUCTANCE (
   POLY, ARCTAN, E-ALPHANET)
delta_t=Ton/(N);              %
   DISCRETIZATION OF THE TIME
   SCALE CONSIDERING N STEPS

%INITIALIZATION
i(1)=i_min;                   %
   INITIAL CONDITION FOR THE
   CURRENT
L(1)=INDUCTOR_MODEL(i(1));    %
   CALCULATE INDUCTANCE
   THROUGH THE SELECTED MODEL
t(1)=0;                       %
   INITIAL TIME
%EQ. (18) DISCRETIZATION
for k=1:N

%NEXT STEP CALCULATION
i(k+1)=i(k)+(VL-i(k)*r)*
   delta_t/(L(k));
L(k+1)=INDUCTOR_MODEL(i(k+1));
t(k+1)=t(k)+delta_t;
end
```

References

1. Cristiano, R., Ponce, E., Pagano, D.J., Granzotto, M.: On the Teixeira singularity bifurcation in a DC-DC power electronic converter. Nonlinear Dyn. **96**(2), 1243–1266 (2019). https://doi.org/10.1007/s11071-019-04851-8
2. Avrutin, V., Zhusubaliyev, Z.T., El Aroudi, A.: Non-visible transformations of chaotic attractors due to their ultra-low density in AC-DC power factor correction converters. Nonlinear Dyn. **102**(4), 2905–2924 (2020). https://doi.org/10.1007/s11071-020-06077-5
3. Gao, P., Min, F., Li, C., Zhang, L.: Dynamical analysis of boundary behaviors of current-controlled DC-DC buck converter. Nonlinear Dyn. **106**(3), 2203–2228 (2021). https://doi.org/10.1007/s11071-021-06918-x
4. Azarastemal, S., Hejri, M.: Cascade control system design and stability analysis for a DC-DC boost converter with proportional integral and sliding mode controllers and using singular perturbation theory. Iran. J. Sci. Technol. Trans. Electr. Eng. **45**(4), 1445–1462 (2021). https://doi.org/10.1007/s40998-021-00444-7

5. Biolek, Z., Biolek, D., Biolková, V., Kolka, Z.: Lagrangian and Hamiltonian formalisms for coupled higher-order elements: theory, modeling, simulation. Nonlinear Dyn. **104**(4), 3547–3560 (2021). https://doi.org/10.1007/s11071-021-06525-w
6. Haška, K., Cveticanin, S.M., Zorica, D.: Dissipative and generative fractional electric elements in modeling RC and RL circuits. Nonlinear Dyn. **105**(4), 3451–3474 (2021). https://doi.org/10.1007/s11071-021-06809-1
7. Oliveri, A., Lodi, M., Storace, M.: Nonlinear models of power inductors: a survey. Int. J. Circuit Theory Appl. **50**(1), 2–34 (2022). https://doi.org/10.1002/cta.3147
8. Perdigão, M.S., Trovão, J.P.F., Alonso, J.M., Saraiva, E.S.: Large-signal characterization of power inductors in EV bidirectional DC-DC converters focused on core size optimization. IEEE Trans. Industr. Electron. **62**(5), 3042–3051 (2015). https://doi.org/10.1109/TIE.2015.2402632
9. Kaiser, J., Dürbaum, T.: An overview of saturable inductors: applications to power supplies. IEEE Trans. Power Electron. **36**(9), 10766–10775 (2021). https://doi.org/10.1109/TPEL.2021.3063411
10. Mastromauro, R.A., Liserre, M., Dell'Aquila, A.: Study of the effects of inductor nonlinear behavior on the performance of current controllers for single-phase PV grid converters. IEEE Trans. Industr. Electron. **55**(5), 2043–2052 (2008). https://doi.org/10.1109/TIE.2008.917117
11. Oliveri, A., Di Capua, G., Stoyka, K., Lodi, M., Storace, M., Femia, N.: A power-loss-dependent inductance model for ferrite-core power inductors in switch-mode power supplies. IEEE Trans. Circuits Syst. I Regul. Pap. **66**(6), 2394–2402 (2019). https://doi.org/10.1109/TCSI.2018.2889856
12. Oliveri, A., Lodi, M., Storace, M.: Accurate modeling of inductors working in nonlinear region in switch-mode power supplies with different load currents. In: 2018 15th International Conference on Synthesis, Modeling, Analysis and Simulation Methods and Applications to Circuit Design (SMACD), pp. 233–236 (2018). https://doi.org/10.1109/SMACD.2018.8434871
13. Van den Bossche, A., Cekov Valchev, V.: Inductors and Transformers for Power Electronics, 1st edn. CRC Press, Boca Raton (2005). https://doi.org/10.1201/9781420027280
14. Femia, N., Stoyka, K., Di Capua, G.: Impact of inductors saturation on peak-current mode control operation. IEEE Trans. Power Electron. **35**(10), 10969–10981 (2020). https://doi.org/10.1109/TPEL.2020.2974939
15. Pilato, G., Rizzo, R., Vella, F., Gianpaolo, V.: Intelligent - web search for EMI filter optimization. In: Proceedings of the 13th International Workshop on Fuzzy Logic and Applications (WILF 2021), volume 3074, Vietri sul Mare, Italy (2021)
16. Lee Ozenbaugh, R., Pullen, T.M.: EMI Filter Design, 3rd edn. CRC Press, Boca Raton (2017). https://doi.org/10.1201/b11543
17. Giglia, G., Ala, G., Piazza, M.C.D., Giaconia, G.C., Luna, M., Vitale, G., Zanchetta, P.: Automatic EMI filter design for power electronic converters oriented to high power density. Electronics **7**(1), 1 (2018). https://doi.org/10.3390/electronics7010009
18. Lullo, G., Scirè, D., Vitale, G.: Non-linear inductor modelling for a DC/DC buck converter. Renew. Energy Power Qual. J. **1**(15), 686–693 (2017). https://doi.org/10.24084/repqj15.43
19. Vitale, G., Lullo, G., Scirè, D.: Thermal stability of a DC/DC converter with inductor in partial saturation. IEEE Trans. Industr. Electron. **68**(9), 7985–7995 (2021). https://doi.org/10.1109/TIE.2020.3014580
20. Scirè, D., Rosato, S., Lullo, G., Vitale, G.: A temperature dependent non-linear inductor model for a dc/dc boost converter. In: 2018 15th International Conference on Synthesis, Modeling, Analysis and Simulation Methods and Applications to Circuit Design (SMACD), pp. 237–9 (2018). https://doi.org/10.1109/SMACD.2018.8434880
21. Scirè, D., Rosato, S., Lullo, G., Vitale, G.: Characterization of non-linear inductors including thermal effects for power applications. Renew. Energy Power Qual. J. **1**(16), 728–734 (2018). https://doi.org/10.24084/repqj16.446
22. Scirè, D., Lullo, G., Vitale, G.: Non-linear inductor models comparison for switched-mode power supplies applications. Electronics (2022). https://doi.org/10.3390/electronics11152472
23. Bizzarri, F., Lodi, M., Oliveri, A., Brambilla, A., Storace, M.: A nonlinear inductance model able to reproduce thermal transient in SMPS simulations. In: 2019 IEEE International Symposium on Circuits and Systems (ISCAS), pp. 1–5 (2019). https://doi.org/10.1109/ISCAS.2019.8702418
24. Górecki, K., Detka, K.: Application of average electrothermal models in the spice-aided analysis of boost converters. IEEE Trans. Industr. Electron. **66**(4), 2746–2755 (2019). https://doi.org/10.1109/TIE.2018.2847694
25. Dervenis, N., Alexandridis, G., Stafylopatis, A.: Neural network specialists for inverse spiral inductor design. In: 2018 IEEE 30th International Conference on Tools with Artificial Intelligence (ICTAI), pp. 60–64 (2018). https://doi.org/10.1109/ICTAI.2018.00020
26. Liu, T., Zhang, W., Yu, Z.: Modeling of spiral inductors using artificial neural network. In: Proceedings 2005 IEEE International Joint Conference on Neural Networks, 2005, 4, 2353–2358 (2005) https://doi.org/10.1109/IJCNN.2005.1556269
27. Guillod, T., Papamanolis, P., Kolar, J.W.: Artificial neural network (ANN) based fast and accurate inductor modeling and design. IEEE Open J. Power Electron. **1**, 284–299 (2020). https://doi.org/10.1109/OJPEL.2020.3012777
28. Rasekh, N., Wang, J., Yuan, X.: Artificial neural network aided loss maps for inductors and transformers. IEEE Open J. Power Electron. **3**, 886–898 (2022). https://doi.org/10.1109/OJPEL.2022.3223936
29. Burrascano, P., Di Capua, G., Laureti, S., Ricci, M.: Neural models of ferrite inductors non-linear behavior. In: 2019 IEEE International Symposium on Circuits and Systems (ISCAS), pp. 1–5 (2019). https://doi.org/10.1109/ISCAS.2019.8702466
30. Cirasa, A., Pilato, G., Sorbello, F., Vassallo, G.: Eαnet: A neural solution for web pages classification. In: Proceedings of 4th World MultiConference on Systemics, Cybernetics and Informatics-SCI, pp. 23–26 (2000)
31. Gaglio, S., Pilato, G., Sorbello, F., Vassallo, G.: Using the hermite regression formula to design a neural architecture with automatic learning of the "hidden" activation functions. In: Evelina, L., Paola, M. (eds.)AI*IA 99: Advances in Arti-

ficial Intelligence, pp. 226–237. Berlin: Springer Berlin Heidelberg (2000)
32. Pilato, G., Sorbello, F., Vassallo, G.: An innovative way to measure the quality of a neural network without the use of a test set. J. Adv. Comput. Intell. Intell. Inform. **5**(1), 31–36 (2001). https://doi.org/10.20965/jaciii.2001.p0031
33. Siniscalchi, S.M., Li, J., Pilato, G., Vassallo, G., Clements, M.A., Gentile, A., Sorbello, F.: Application of eαnets to feature recognition of articulation manner in knowledge-based automatic speech recognition. Neural Nets **3931**, 140–146 (2006). https://doi.org/10.1007/11731177_21
34. Powell, M.J.: Restart procedures for the conjugate gradient method. Math. Program. **12**(1), 241–254 (1977). https://doi.org/10.1007/BF01593790
35. Friedman, J.H.: Multivariate adaptive regression splines. Ann. Stat. **19**(1), 1–67 (1991). https://doi.org/10.1214/aos/1176347963
36. Minor, J.M.: Parity with two layer feedforward nets. Neural Netw. **6**(5), 705–707 (1993). https://doi.org/10.1016/S0893-6080(05)80114-5
37. Fahlman, S. E., Lebiere, C.: The cascade-correlation learning architecture. In: Touretzky, D. (ed) Advances in Neural Information Processing Systems, vol. 2, pp. 524–532. Morgan Kaufmann Publishers Inc, San Francisco (1989)
38. Hwang, J.-N., Shyh-Rong Lay, M., Maechler, R.D.M., Schimert, J.: Regression modeling in back-propagation and projection pursuit learning. IEEE Trans. Neural Netw. **5**(3), 342–353 (1994). https://doi.org/10.1109/72.286906
39. Cirasa, A., Pilato, G., Sorbello, F., Vassallo, G.: An enhanced version of the eαnet architecture. In: Proceedings of AI*IA Workshop of Robotics Parma, Italy (1999)
40. Drougge , E., Wroldsen, J.: A robust algorithm for pruning neural networks. Gjovik College Preprint (1994)
41. Lodi, M., Oliveri, A., Storace, M.: Behavioral models for ferrite-core inductors in switch-mode DC-DC power supplies: a survey. In: 2019 IEEE 5th International forum on Research and Technology for Society and Industry (RTSI), pp. 242–247 (2019). https://doi.org/10.1109/RTSI.2019.8895593
42. Ventimiglia, M., Sciré, D., Lullo, G., Vitale, G.: A measurement system for power inductors in non-linear operating conditions. In: 2021 IEEE 30th International Symposium on Industrial Electronics (ISIE), pp. 1–6 (2021). https://doi.org/10.1109/ISIE45552.2021.9576289
43. Scirè, D., Vitale, G., Ventimiglia, M., Lullo, G.: Nonlinear inductors characterization in real operating conditions for power density optimization in SMPS. Energies (2021). https://doi.org/10.3390/en14133924
44. Scirè, D., Lullo, G., Vitale, G.: Design and modeling of an interleaving boost converter with quasi-saturated inductors for electric vehicles. In: 2020 AEIT International Conference of Electrical and Electronic Technologies for Automotive (AEIT AUTOMOTIVE), pp. 1–6 (2020). https://doi.org/10.23919/AEITAUTOMOTIVE50086.2020.9307424
45. Roberto, S.F., Sciré, D., Lullo, G., Vitale, G.: Equivalent circuit modelling of ferrite inductors losses. In: 2018 IEEE 4th International Forum on Research and Technology for Society and Industry (RTSI), pp. 1–4 (2018). https://doi.org/10.1109/RTSI.2018.8548450
46. Pedregosa, F., Varoquaux, G., Gramfort, A., Michel, V., Thirion, B., Grisel, O., Blondel, M., Prettenhofer, P., Weiss, R., Dubourg, V., Vanderplas, J., Passos, A., Cournapeau, D., Brucher, M., Perrot, M., Duchesnay, E.: Scikit-learn: machine learning in Python. J. Mach. Learn. Res. **12**, 2825–2830 (2011)
47. Scirè, D., Lullo, G., Vitale, G.: EMI filter re-design in a SMPS with inductor in saturation. In: 2021 IEEE 15th International Conference on Compatibility, Power Electronics and Power Engineering (CPE-POWERENG), pp. 1–7 (2021). https://doi.org/10.1109/CPE-POWERENG50821.2021.9501176